Castro et al. *NPG Asia Materials* (2020) 12:35
https://doi.org/10.1038/s41427-020-0214-y

NPG Asia Materials

ARTICLE Open Access

# Machine-learning-guided discovery of the gigantic magnetocaloric effect in $HoB_2$ near the hydrogen liquefaction temperature

Pedro Baptista de Castro[1,2], Kensei Terashima[1], Takafumi D Yamamoto[1], Zhufeng Hou[3], Suguru Iwasaki[1], Ryo Matsumoto[1,2], Shintaro Adachi[1], Yoshito Saito[1,2], Peng Song[1,2], Hiroyuki Takeya[1] and Yoshihiko Takano[1,2]

**Abstract**

Magnetic refrigeration exploits the magnetocaloric effect, which is the entropy change upon the application and removal of magnetic fields in materials, providing an alternate path for refrigeration other than conventional gas cycles. While intensive research has uncovered a vast number of magnetic materials that exhibit a large magnetocaloric effect, these properties remain unknown for a substantial number of compounds. To explore new functional materials in this unknown space, machine learning is used as a guide for selecting materials that could exhibit a large magnetocaloric effect. By this approach, $HoB_2$ is singled out and synthesized, and its magnetocaloric properties are evaluated, leading to the experimental discovery of a gigantic magnetic entropy change of 40.1 J $kg^{-1}$ $K^{-1}$ (0.35 J $cm^{-3}$ $K^{-1}$) for a field change of 5 T in the vicinity of a ferromagnetic second-order phase transition with a Curie temperature of 15 K. This is the highest value reported so far, to the best of our knowledge, near the hydrogen liquefaction temperature; thus, $HoB_2$ is a highly suitable material for hydrogen liquefaction and low-temperature magnetic cooling applications.

## Introduction

The magnetocaloric effect (MCE) is a promising approach for environmentally friendly cooling, as it does not depend on the use of hazardous or greenhouse gases[1–4] while being, in principle, able to attain a higher thermodynamic cycle efficiency[1,5,6], where this cycle makes use of the magnetic entropy change ($\Delta S_M$) and the adiabatic temperature change ($\Delta T_{ad}$) through the application/removal of a magnetic field in a material. Since large values of $\Delta S_M$ are usually achieved near the magnetic transition temperature ($T_{mag}$), the working temperature range is confined around the $T_{mag}$ of the material. The MCE was first used to achieve ultralow cryogenic temperatures (below 1 K)[7] and has been widely used for liquefying He[8], where the main component is the gadolinium gallium garnet $Gd_3Ga_5O_{12}$(GGG)[9]. The remarkable discovery of giant MCEs near room temperature in families of materials such as $Gd_5Si_2Ge_2$[10], $La(Fe,Si)_{13}$[11], and $MnFeP_{1-x}As_x$[3] shifted the main focus of research into finding and tuning new materials, such as NiMnIn Heusler alloys[12], working around this temperature range due to its potential economic and environmental impact[2].

On the other hand, there is an increasing demand for cooling systems around the hydrogen liquefaction temperature ($T = 20.3$ K), since liquid hydrogen is one of the candidates for green fuel in the substitution of petroleum-based fuels[13] and is also widely needed as a rocket propellant and space exploration fuel[14,15]. It has been shown that MCE-based refrigerator prototypes are highly appropriate for this task[5]. In this context, the discovery of

Correspondence: Pedro Baptista de Castro (CASTRO.Pedro@nims.go.jp) or Kensei Terashima (TERASHIMA.Kensei@nims.go.jp) or Yoshihiko Takano (TAKANO.Yoshihiko@nims.go.jp)
[1]National Institute for Materials Science, 1-2-1 Sengen, Tsukuba, Ibaraki 305-0047, Japan
[2]University of Tsukuba, 1-1-1 Tennodai, Tsukuba, Ibaraki 305-8577, Japan
Full list of author information is available at the end of the article

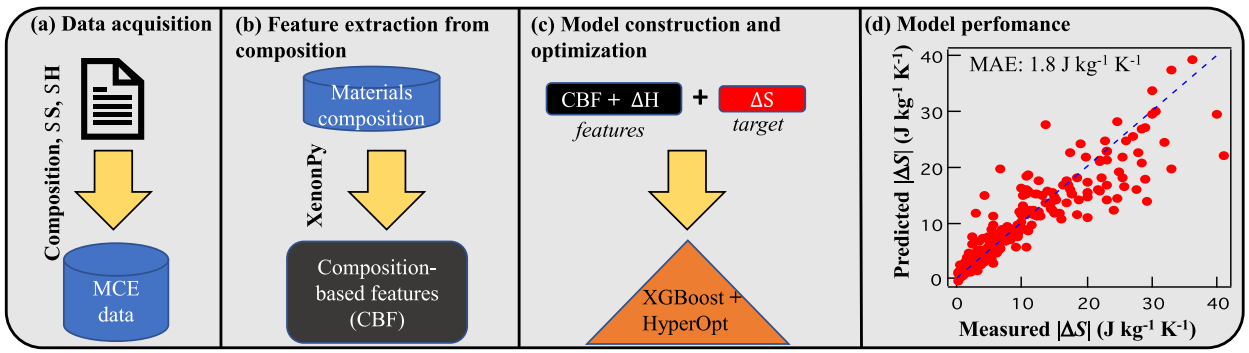


**Fig. 1 Diagram for the construction of the machine-learning model for MCE. a** As a first step, magnetocaloric relevant papers were screened from the MagneticMaterials[28] database, followed by the extraction of MCE data from these papers and from a previous review[2]. **b** Features based on compositions were extracted by the XenonPy[30] python package and used in conjunction with the reported field change values. **c** Model optimization was achieved using the HyperOpt package by minimizing the MAE score. **d** The model performance was evaluated by a comparison of the predicted $\Delta S_M$ values obtained from the constructed model with the reported ones for ~300 unseen materials by the model, where an MAE of 1.8 J kg$^{-1}$ K$^{-1}$ was achieved.

materials exhibiting a remarkable MCE response near the liquefaction temperature of hydrogen is highly anticipated.

One way of tackling this problem is by taking advantage of data-driven approaches, such as machine learning (ML), as it has been successfully applied to cases ranging from the modeling of new superconductors[16,17] and thermoelectric materials[18,19] to the prediction of the synthesizability of inorganic materials[20]. In the case of magnetism and magnetic materials, this approach has been successfully applied to the prediction of the Curie temperature ($T_C$) of ferromagnets[21,22] and to the design of new permanent magnets[23,24], and new magnetic Heusler-type alloys[25]. However, for MCE materials, this kind of approach has not been extensively tried, being limited to first-principles calculations, which have been restricted to non-rare-earth systems[26].

As a result of extensive research on magnetocaloric materials, accumulated data regarding the MCE properties of diverse types of materials have been made accessible in, e.g., recent reviews[2,27]. In addition, recent efforts to extract the $T_{mag}$ of materials from research reports have led to the creation of MagneticMaterials[28], an autogenerated database of magnetic materials built by natural language processing that contains a vast number of materials whose magnetic properties are known. Among these materials, there are still many regarding which their MCE properties have not been evaluated. Therefore, by combining the known and unknown data, a data-driven trial can be used as a guide to find materials with a high MCE response.

In this work, we attempt a novel approach by using ML to screen and select compounds that might exhibit a high MCE performance, focusing on ferromagnetic materials with a $T_C$ of ~20 K. For this purpose, we collected data from the literature[2,28] to train an ML algorithm in an attempt to predict the $\Delta S_M$ of a given material composition. By this method, we singled out $HoB_2$ ($T_C = 15$ K[29]) as a possible candidate, leading us to the experimental discovery of a gigantic MCE of $|\Delta S_M| = 40.1$ J kg$^{-1}$ K$^{-1}$ (0.35 J cm$^{-3}$ K$^{-1}$) for a field change of 5 T in this material.

## Materials and methods

### Data acquisition and machine-learning model building

Figure 1 shows a schematic flow exhibiting the construction of the machine-learned model for MCE materials. We started with the screening of magnetocaloric relevant papers from the MagneticMaterials[28] database and gathered the reported MCE properties from a total of 219 different journal titles contained therein, mostly focusing on the reported peak values of $|\Delta S_M|$ for a given field change ($\mu_0 \Delta H$) of a given material composition, combining these data with the data available in a recent review[2] by Franco et. al. To remove any possible duplicates in the final dataset, the materials that contained more than one value of $|\Delta S_M|$ for a given $\mu_0 \Delta H$ had their values averaged, and this average was used as the final value. Last, we selected the data within the range of $\mu_0 \Delta H \leq 5$ for compatibility with our experimental setup, obtaining 1644 data points that were used for the model construction.

To predict the MCE property, namely, $|\Delta S_M|$, of a material given its chemical formula, we used three different types of features in the final feature vector (Table 1). The first type is the composite-type features that were extracted using the XenonPy[30] python package. These composite features were obtained by combining all 58 element-level properties of the atomic species contained in a chemical composition, such as the atomic mass of the constituent elements, density, etc., which are readily available inside the XenonPy package (their complete list

**Table 1 Dimension size of each feature vector used in the construction of the machine-learning model for the construction of the final feature vector.**

| Feature type | Dimension |
|---|---|
| Composite features (the combination of elemental-based properties of the atomic species contained in the chemical formula by the featurizers) | 343 |
| Counting feature (amount of each atomic species contained in the chemical formula) | 64 |
| Experimental values of field change | 1 |

is given in Supplementary Information Section 1). To generate these composite features, seven different featurizers implemented in XenonPy were used: weighted average, weighted sum, weighted variance, geometric mean, harmonic mean, max pooling and min pooling (their mathematical definitions are given in Supplementary Information Section 1), with a total of 406 composite features being obtained. The second type is the amount of each atomic species present in each compound chemical formula, restricted to the elements between $^{1}$H and $^{94}$Pu, which is also readily implemented in XenonPy using the counting featurizer. The last feature used is the experimental applied field change, which is obtained directly from the experimental reports. After generating the features with XenonPy (composite features + counting featurizer), yielding a total of 500 features, we removed the features of which all values were zero, infinite or divided by zero (not a number, NaNs), ending with 343 composite features, 64 counting features and $\Delta H$, totaling 408 features in the final feature vector. We summarize them in the Table 1 and show all the features used in Supplementary Information Section 1.

After the extracted features were combined with the reported values of $|\Delta S_M|$, a gradient boosted tree algorithm implemented in the XGBoost[31] package was trained over 80% of the total data. To further improve the prediction power, model selection and hyperparameter tuning were performed by using a Bayesian optimization technique implemented in the HyperOpt[32] package by minimizing the mean absolute error (MAE) tenfold cross-validation score. The resulting model achieved an MAE of 1.8 J kg$^{-1}$ K$^{-1}$ when tested on the remaining 20% of the data. For more details of the hyperparameters used, model building and performance comparison with other machine-learning algorithms, refer to Supplementary Information Section 2.

After the model construction, we examined 818 unknown $\Delta S_M$ text-mined compositions with $T_C \leq 150$ K contained in the MagneticMaterials[28] database using the following criteria: the predicted value of $|\Delta S_M|$ is higher than 15 J kg$^{-1}$ K$^{-1}$, alloys only, the chemical composition contains heavier rare earth elements (Gd-Er), and no toxic elements, such as arsenic, are present. As a result, $HoB_2$ ($AlB_2$ type, space group $P6/mmm$) was selected, as it had the highest predicted $|\Delta S_M|$ (16.3 J kg$^{-1}$ K$^{-1}$) for a field change of 5 T among the binary candidates, followed by its synthesis and the characterization of its MCE properties.

### Sample synthesis

Polycrystalline samples of $HoB_2$ were synthesized by an arc-melting process in a water-cooled copper heath arc furnace. Stoichiometric amounts of Ho (99.9% purity) and B (99.5% purity) were arc melted under an Ar atmosphere. To ensure homogeneity, the sample was flipped and melted several times, followed by annealing in an evacuated quartz tube at 1000 °C for 24 hours and water quenching. X-ray diffraction was carried out, and $HoB_2$ was confirmed as the main phase structure (see Supplementary Information Section 3).

### Magnetic measurements

Magnetic measurements were carried out by a superconducting quantum interference device (SQUID) magnetometer contained in the MPMS XL (Magnetic Property Measurement System, Quantum Design).

### Specific heat measurement

Specific heat measurement was carried out in a PPMS (Physical Property Measurement System, Quantum Design) equipped with a heat capacity option.

## Results

Figure 2a shows the isofield magnetization ($M$–$T$) curve of the synthesized polycrystalline $HoB_2$ for an applied field of 0.01 T. $HoB_2$ orders ferromagnetically at $T_C =$ 15 K without thermal hysteresis, consistent with a previous report[29], and the isothermal magnetization ($M$–$H$) at $T = 5$ K, shown in Fig. 2b, reveals a negligible magnetic hysteresis. A vast number of $M$–$T$ curves for fields ranging from 0–5 T were measured (Fig. 2c) to evaluate $|\Delta S_M|$ (Fig. 2d) using the Maxwell relation:

$$\Delta S_M = \mu_0 \int_0^H \left(\frac{\partial M}{\partial T}\right)_H dH \quad (1)$$

For a field change of 5 T, we obtained $|\Delta S_M| = 40.1$ J kg$^{-1}$ K$^{-1}$ in the vicinity of $T_C$.

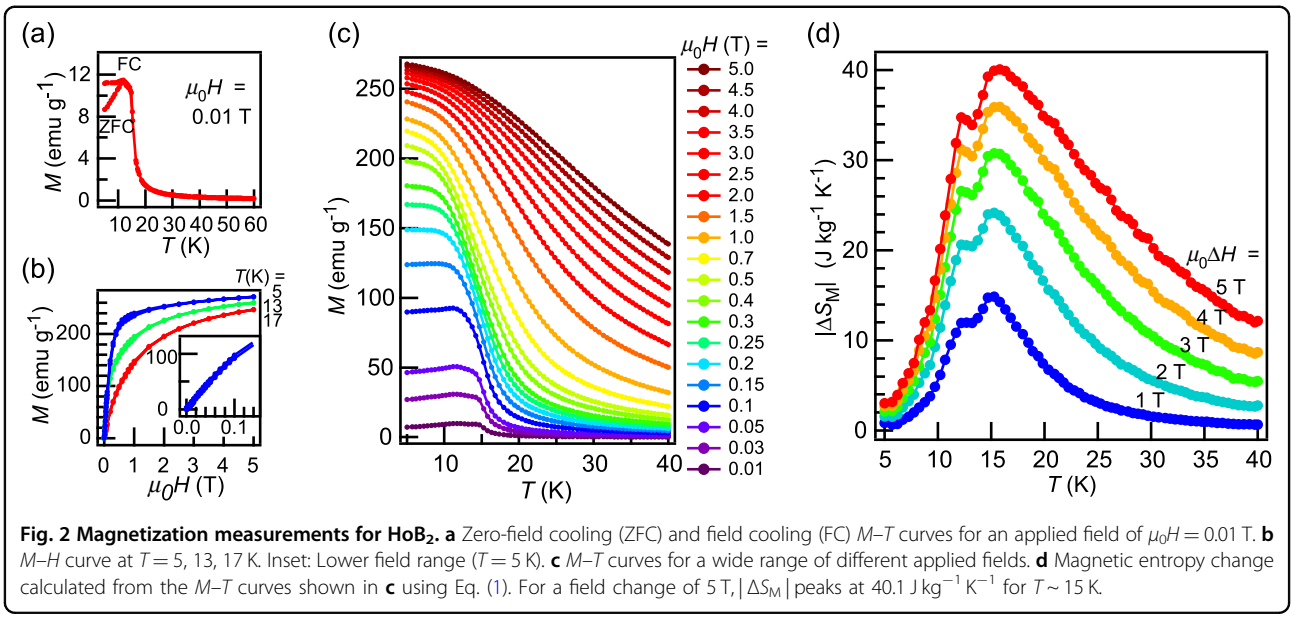


**Fig. 2 Magnetization measurements for $HoB_2$. a** Zero-field cooling (ZFC) and field cooling (FC) *M–T* curves for an applied field of $\mu_0H = 0.01$ T. **b** *M–H* curve at $T = 5$, 13, 17 K. Inset: Lower field range ($T = 5$ K). **c** *M–T* curves for a wide range of different applied fields. **d** Magnetic entropy change calculated from the *M–T* curves shown in **c** using Eq. (1). For a field change of 5 T, $|\Delta S_M|$ peaks at 40.1 J kg$^{-1}$ K$^{-1}$ for $T \sim 15$ K.

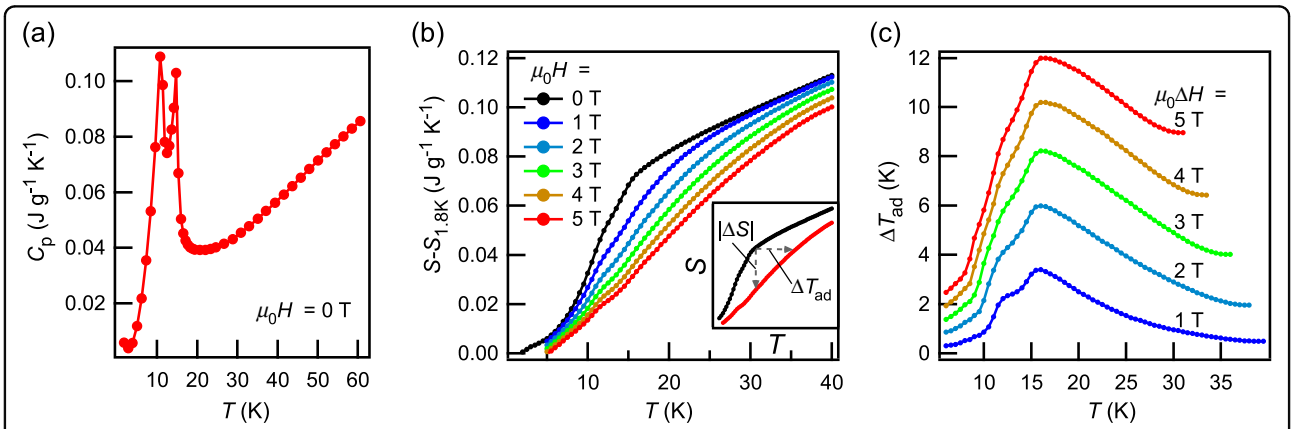


**Fig. 3 Calorimetric properties of $HoB_2$. a** Zero-field-specific heat of $HoB_2$. **b** Entropy as a function of temperature obtained from the zero-field-specific heat measurement. Entropy curves under magnetic fields are obtained by combining the entropy curve at 0 T with the $|\Delta S_M|$ values of Fig. 2d. The inset shows the definitions of $\Delta S$ and $\Delta T_{ad}$. **c** $\Delta T_{ad}$ calculated from **b**.

For further evaluation of the MCE performance of $HoB_2$, a specific heat measurement was carried out, as shown in Fig. 3a, revealing the presence of two peaks: one in a lower temperature regime (≈11 K) and a second at $T_C = 15$ K. The first peak, which can also be seen in the $|\Delta S_M|$ curves (Fig. 2c), is probably due to a spin-reorientation transition similar to that observed in the related compound $DyB_2$[33], but at this stage, we keep its physical origin an open question to be clarified in a future work. To obtain the entropy curves $S(T)$ at different applied fields (Fig. 3b), the zero-field entropy curve $[S(\mu_0H = 0\,\mathrm{T},\ T)]$ was first calculated using the data from Fig. 3a through the following equation:

$$S(T) = \int_{T_{\min}}^{T} \frac{C}{T} dT \qquad (2)$$

where $T_{\min} = 1.8$ K, and the $|\Delta S_M|$ values obtained from the magnetization measurements were added to the zero-field entropy curve (shown as the black dots in Fig. 3b). For more details about this method, see Supplementary Information Section 4. The adiabatic temperature change, $\Delta T_{ad}$, defined as $\Delta T_{ad}[T_i,\ \mu_0\Delta H = \mu_0(H_f - H_0)] = T_f(S_i,\ \mu_0H_f \neq 0) - T_i(S_i,\ \mu_0H_0 = 0\,\mathrm{T})$, was obtained from Fig. 3b

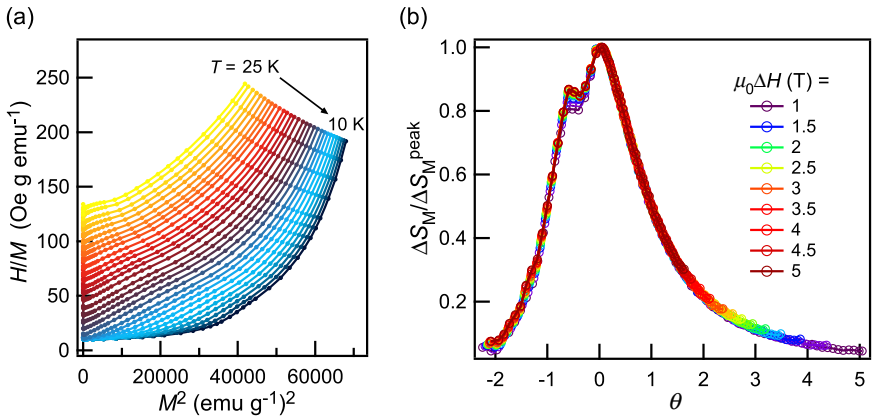


**Fig. 4 Analyses regarding the order of the magnetic transition in $HoB_2$. a** Arrott plots obtained from the *M-T* curves shown in Fig. 2c. **b** Normalized entropy curve as a function of the reduced temperature $\theta$. All curves collapse perfectly into each other, indicating a possible SOPT for the ferromagnetic transition at $T_C = 15$ K.

by first interpolating the entropy curves with the applied field, followed by taking the adiabatic difference with respect to the zero-field entropy curve (see inset of Fig. 3b). The maximum obtained $\Delta T_{ad}$, shown in Fig. 3c, was 12 K for a field change of 5 T.

To further understand the ferromagnetic transition at $T_C = 15$ K, Arrott plots were constructed (Fig. 4a), showing that all the plot slopes are positive. According to the Banerjee criterion[34], this behavior is characteristic of a second-order phase transition (SOPT). Furthermore, a so-called universal scaling curve (Fig. 4b) proposed by earlier works[35–38], which depicts the normalized entropy change $|\Delta S_M| / |\Delta S_M^{peak}|$ as a function of a normalized temperature $\theta$, was built, where $\theta$ is defined as:

$$\theta = \begin{cases} \frac{T_C - T}{T_{r_1} - T_C}, T \leq T_C \\ \frac{T - T_C}{T_{r_2} - T_C}, T > T_C \end{cases}$$

where $T_{r1}$ and $T_{r2}$ are reference temperatures, for which $|\Delta S_M| / |\Delta S_M^{peak}| = 0.5$. For the SOPT, these curves are expected to collapse into each other, exhibiting a universal behavior, while for first-order transitions (FOPTs), a nonuniversal and dispersive behavior between the curves appears.

In the obtained normalized entropy curves (Fig. 4b), the former behavior is observed as all the normalized entropy curves collapse into each other. Although a divergence at $\theta = -1$ is observed, it can be associated with the presence of the second magnetic transition at lower temperatures, similarly observed for materials that exhibit more than one magnetic transition[39,40]. The absence of magnetic and thermal hysteresis coupled with the observation of a universal entropy curve suggests that the transition at $T_C = 15$ K is of second order. All the above analyses are also in accordance with a second-order transition for the low-temperature transition (~11 K), but further experiments are required to conclude the nature and origin of this transition.

## Discussion

To compare the performance of $HoB_2$ with that of other candidates for refrigeration applications near the hydrogen liquefaction temperature, such as $ErAl_2$[5], representative large $|\Delta S_M|$ (for $\mu_0 \Delta H = 5$ T) materials at $\sim T = 20$ K are displayed in Table 2. We also show the values of $|\Delta S_M|$ in units of J cm$^{-3}$ K$^{-1}$, which is the ideal unit from the application point of view[6,27].

Except for single-crystalline $ErCo_2$, which exhibits an FOPT, $HoB_2$ manifests the largest $|\Delta S_M|$ (in both J kg$^{-1}$ K$^{-1}$ and J cm$^{-3}$ K$^{-1}$) and $\Delta T_{ad}$ for a field change of 5 T around the hydrogen liquefaction temperature. Among materials whose $|\Delta S_M|$ value peaks around their SOPT, it also exhibits the largest volumetric entropy change ($|\Delta S_M|$ in J cm$^{-3}$ K$^{-1}$) in the temperature range from liquid helium (4.2 K) to liquid nitrogen (77 K). For a more comprehensive comparison of materials between liquid helium and liquid nitrogen range, see Supplementary Information Section 5.

It is important to recall that this gigantic magnetocaloric effect is observed in the vicinity of an SOPT at $T_C = 15$ K. SOPT materials have the advantage of being free of magnetic and thermal hysteresis while having broader $\Delta S_M$ peaks. Thus, they are likely to be more suitable for refrigeration purposes than FOPT materials, which tends to be plagued by these problems[1,41]. In other words, $HoB_2$ is a high-performance candidate material for low-temperature magnetic refrigeration applications such as hydrogen liquefaction.

## Conclusions

In summary, by using a machine-learning aided approach, we have successfully unveiled a ferromagnet

**Table 2 Comparison of MCE-related properties in $HoB_2$ and other materials exhibiting large magnetocaloric response around the liquefaction temperature of hydrogen for a field change of 5 T.**

| Materials | $T_{mag}$ (K) | $\|\Delta S_M\|$ (J kg$^{-1}$ K$^{-1}$) | $\|\Delta S_M\|$ (J cm$^{-3}$ K$^{-1}$) | $\Delta T_{ad}$ (K) | Transition type | References |
|---|---|---|---|---|---|---|
| $HoB_2$ | 15 | 40.1 | 0.35 | 12 | SOPT | This work |
| EuS | 18.2 | 37 | 0.21 | 10.4 | SOPT | [42] |
| $ErAl_2$ | 14 | 36 | 0.22 | 11.1 | SOPT | [43] |
| $ErCo_2$ | 30 | 36 | 0.37 | 9.5 | FOPT | [44] |
| TmGa | 15 | 34.2 | 0.30 | 9.1 | SOPT | [45] |
| $HoAl_2$ | 27 | 28.8 | 0.17 | * | SOPT | [46] |
| $GdCoC_2$ | 15 | 28.4 | 0.23 | * | SOPT | [47] |
| HoN | 18 | 28.2 | 0.29 | * | SOPT | [48] |
| $HoNi_2$ | 13.9 | 26.1 | 0.27 | 8.7 | SOPT | [49] |
| ErFeSi | 22 | 23.5 | 0.18 | 7.1 | SOPT | [50] |

The data was taken from the refs. [42–50] in J kg$^{-1}$ K$^{-1}$ and also converted into J cm$^{-3}$ K$^{-1}$ by using the ideal density according to the AtomWork[51] database. Asterisk (*) indicates an unreported value.

that will manifest a high magnetocaloric performance with a transition temperature around the hydrogen liquefaction temperature. By synthesizing and evaluating its MCE properties, we discovered a gigantic magnetocaloric effect of $HoB_2$ in the vicinity of an SOPT at $T_C = 15$ K, where the maximum obtained magnetocaloric entropy change was 40.1 J kg$^{-1}$ K$^{-1}$ (0.35 J cm$^{-3}$ K$^{-1}$) with an adiabatic temperature change of 12 K for a field change of 5 T, the highest value reported until now, to the best of our knowledge, for materials working near the liquefaction temperature of hydrogen.

**Acknowledgements**
We acknowledge fruitful discussions with Mohammed ElMassalami. This work was supported by the JST-Mirai Program Grant No. JPMJMI18A3, JSPS KAKENHI Grant No. 19H02177, and JST CREST Grant No. JPMJCR16Q6. P.B.C. also acknowledges scholarship support from the Ministry of Education, Culture, Sports, Science and Technology (MEXT), Japan.

**Author details**
[1]National Institute for Materials Science, 1-2-1 Sengen, Tsukuba, Ibaraki 305-0047, Japan. [2]University of Tsukuba, 1-1-1 Tennodai, Tsukuba, Ibaraki 305-8577, Japan. [3]State Key Laboratory of Structural Chemistry, Fujian Institute of Research on the Structure of Matter, Chinese Academy of Sciences, 350002 Fuzhou, China

**Author contributions**
Y.T. conceived the project idea. P.B.C. performed the data acquisition, preprocessing, machine-learning model building, and material prediction with the assistance of H.Z. P.B.C. and K.T. performed the sample synthesis with the assistance of H.T. K.T. carried out the magnetization measurements and heat capacity measurements with T.D. Y.K.T. and P.B.C. analyzed the experimental data. P.B.C. and K.T. wrote the manuscript. All authors discussed the manuscript together.

**Conflict of interest**
The authors declare that they have no conflict of interest.



**Supplementary information** is available for this paper at https://doi.org/10.1038/s41427-020-0214-y.

Received: 23 October 2019 Revised: 19 February 2020 Accepted: 5 March 2020.
Published online: 12 May 2020

**References**

1. Franco, V., Blázquez, J. S., Ingale, B. & Conde, A. The magnetocaloric effect and magnetic refrigeration near room temperature: materials and models. *Annu. Rev. Mater. Res.* **42**, 305–342 (2012).
2. Franco, V. et al. Magnetocaloric effect: from materials research to refrigeration devices. *Prog. Mater. Sci.* **93**, 112–232 (2018).
3. Tegus, O., Brück, E., Buschow, K. H. J. & De Boer, F. R. Transition-metal-based magnetic refrigerants for room-temperature applications. *Nature* **415**, 150–152 (2002).
4. Gutfleisch, O. et al. Magnetic materials and devices for the 21st century: stronger, lighter, and more energy efficient. *Adv. Mater.* **23**, 821–842 (2011).
5. Numazawa, T., Kamiya, K., Utaki, T. & Matsumoto, K. Magnetic refrigerator for hydrogen liquefaction. *Cryog. (Guildf.).* **62**, 185–192 (2014).
6. Gottschall, T. et al. Making a cool choice: the materials library of magnetic refrigeration. *Adv. Energy Mater.* **9**, 1901322 (2019).
7. Giauque, W. F. & MacDougall, D. P. Attainmentof temperatures below 1° absolute by demagnetization of Gd2(SO4)3·8H2O. *Phys. Rev. J. Arch.* **43**, 768–768 (1933).
8. McMichael, R. D., Ritter, J. J. & Shull, R. D. Enhanced magnetocaloric effect in $Gd_3Ga_{5-x}Fe_xO_{12}$. *J. Appl. Phys.* **73**, 6946–6948 (1993).
9. Levitin, R. Z., Snegireva, V. V., Kopylov, A. V., Lagutin, A. S. & Gerber, A. Magnetic method of magnetocaloric effect determination in high pulsed magnetic fields. *J. Magn. Magn. Mater.* **170**, 223–227 (1997).
10. Pecharsky, V. K. & Gschneidner, K. A. Giant magnetocaloric effect in $Gd_5(Si_2Ge_2)$. *Phys. Rev. Lett.* **78**, 4494–4497 (1997).
11. Hu, F. X. et al. Influence of negative lattice expansion and metamagnetic transition on magnetic entropy change in the compound $LaFe_{11.4}Si_{1.6}$. *Appl. Phys. Lett.* **78**, 3675–3677 (2001).
12. Singh, S. et al. Large magnetization and reversible magnetocaloric effect at the second-order magnetic transition in Heusler materials. *Adv. Mater.* **28**, 3321–3325 (2016).

13. Jones, L. W. Liquid hydrogen as a fuel for the future. *Science* **174**, 367–370 (1971).
14. Shirron, P. J. Applications of the magnetocaloric effect in single-stage, multi-stage and continuous adiabatic demagnetization refrigerators. *Cryog. (Guildf.)*. **62**, 130–139 (2014).
15. Chato, D. Cryogenic technology development for exploration missions. In: *45th AIAA Aerospace Sciences Meeting and Exhibit* (American Institute of Aeronautics and Astronautics, 2007). https://doi.org/10.2514/6.2007-953.
16. Stanev, V. et al. Machine learning modeling of superconducting critical temperature. *NPJ Comput. Mater.* **4**, 29 (2018).
17. Matsumoto, R. et al. Two pressure-induced superconducting transitions in $SnBi_2Se_4$ explored by data-driven materials search: new approach to developing novel functional materials including thermoelectric and superconducting materials. *Appl. Phys. Express* **11**, 093101 (2018).
18. Sparks, T. D., Gaultois, M. W., Oliynyk, A., Brgoch, J. & Meredig, B. Data mining our way to the next generation of thermoelectrics. *Scr. Mater.* **111**, 10–15 (2016).
19. Matsumoto, R. et al. Data-driven exploration of new pressure-induced superconductivity in $PbBi_2Te_4$. *Sci. Technol. Adv. Mater.* **19**, 909–916 (2018).
20. Aykol, M. et al. Network analysis of synthesizable materials discovery. *Nat. Commun.* **10**, 2018 (2019).
21. Dam, H. C. et al. Important descriptors and descriptor groups of curie temperatures of rare-earth transition-metal binary alloys. *J. Phys. Soc. Jpn.* **87**, 113801 (2018).
22. Nelson, J. & Sanvito, S. Predicting the Curie temperature of ferromagnets using machine learning. *Phys. Rev. Mater.* **3**, 104405 (2019).
23. Möller, J. J., Körner, W., Krugel, G., Urban, D. F. & Elsässer, C. Compositional optimization of hard-magnetic phases with machine-learning models. *Acta Mater.* **153**, 53–61 (2018).
24. Körner, W., Krugel, G., Urban, D. F. & Elsässer, C. Screening of rare-earth-lean intermetallic 1-11 and 1-11-X compounds of $YNi_9In_2$-type for hard-magnetic applications. *Scr. Mater.* **154**, 295–299 (2018).
25. Sanvito, S. et al. Accelerated discovery of new magnets in the Heusler alloy family. *Sci. Adv.* **3**, e1602241 (2017).
26. Bocarsly, J. D. et al. A Simple computational proxy for screening magnetocaloric compounds. *Chem. Mater.* **29**, 1613–1622 (2017).
27. Gschneidner, A., Pecharsky, V. K. & Tsokol, A. O. Recent developments in magnetocaloric materials. *Rep. Prog. Phys.* **68**, 1479–1539 (2005).
28. Court, C. J. & Cole, J. M. Auto-generated materials database of Curie and Néel temperatures via semi-supervised relationship extraction. *Sci. Data* **5**, 180111 (2018).
29. Roger, J. et al. The ternary RE-Si-B systems (RE = Dy, Ho, Er and Y) at 1270 K: solid state phase equilibria and magnetic properties of the solid solution $REB_{2-x}Si_x$ (RE = Dy and Ho). *J. Alloy. Compd.* **417**, 72–84 (2006).
30. Yamada, H. et al. Predicting materials properties with little data using shotgun transfer learning. *ACS Cent. Sci.* (2019) https://doi.org/10.1021/acscentsci.9b00804.
31. Chen, T. & Guestrin, C. XGBoost. In Proceedings of the 22nd ACM SIGKDD International Conference on Knowledge Discovery and Data Mining - KDD '16 785–794 (ACM Press, 2016) https://doi.org/10.1145/2939672.2939785.
32. Bergstra, J., Komer, B., Eliasmith, C., Yamins, D. & Cox, D. D. Hyperopt: a Python library for model selection and hyperparameter optimization. *Comput. Sci. Discov.* **8**, 014008 (2015).
33. Meng, H. et al. Reversible magnetocaloric effect and refrigeration capacity enhanced by two successive magnetic transitions in DyB2. *Sci. China Technol. Sci.* **55**, 501–504 (2012).
34. Banerjee, B. K. On a generalised approach to first and second order magnetic transitions. *Phys. Lett.* **12**, 16–17 (1964).
35. Franco, V., Blázquez, J. S. & Conde, A. Field dependence of the magnetocaloric effect in materials with a second order phase transition: a master curve for the magnetic entropy change. *Appl. Phys. Lett.* **89**, 222512 (2006).
36. Franco, V., Conde, A., Romero-Enrique, J. M. & Blázquez, J. S. A universal curve for the magnetocaloric effect: an analysis based on scaling relations. *J. Phys. Condens. Matter* **20**, 285207 (2008).
37. Franco, V. & Conde, A. Scaling laws for the magnetocaloric effect in second order phase transitions: From physics to applications for the characterization of materials. *Int. J. Refrig.* **33**, 465–473 (2010).
38. Bonilla, C. M. et al. Universal behavior for magnetic entropy change in magnetocaloric materials: An analysis on the nature of phase transitions. *Phys. Rev. B* **81**, 224424 (2010).
39. Zhang, Y. et al. Study of the magnetic phase transitions and magnetocaloric effect in $Dy_2Cu_2In$ compound. *J. Alloy. Compd.* **667**, 130–133 (2016).
40. Yi, Y., Li, L., Su, K., Qi, Y. & Huo, D. Large magnetocaloric effect in a wide temperature range induced by two successive magnetic phase transitions in $Ho_2Cu_2Cd$ compound. *Intermetallics* **80**, 22–25 (2017).
41. Smith, A. et al. Materials challenges for high performance magnetocaloric refrigeration devices. *Adv. Energy Mater.* **2**, 1288–1318 (2012).
42. Li, D. X. et al. Large reversible magnetocaloric effect in ferromagnetic semiconductor EuS. *Solid State Commun.* **193**, 6–10 (2014).
43. Pecharsky, V. K. & Gschneidner, K. A. Jr. Magnetocaloric effect from indirect measurements: Magnetization and heat capacity. *J. Appl. Phys.* **86**, 565–575 (1999).
44. Wada, H., Tanabe, Y., Shiga, M., Sugawara, H. & Sato, H. Magnetocaloric effects of Laves phase $Er(Co_{1-x}Ni_x)_2$ compounds. *J. Alloy. Compd.* **316**, 245–249 (2001).
45. Mo, Z.-J. et al. Low field induced giant magnetocaloric effect in TmGa compound. *Appl. Phys. Lett.* **103**, 52409 (2013).
46. Hashimoto, T. et al. New application of complex magnetic materials to the magnetic refrigerant in an Ericsson magnetic refrigerator. *J. Appl. Phys.* **62**, 3873–3878 (1987).
47. Meng, L. et al. Magnetic properties and giant reversible magnetocaloric effect in $GdCoC_2$. *RSC Adv.* **6**, 74765–74768 (2016).
48. Yamamoto, T. A., Nakagawa, T., Sako, K., Arakawa, T. & Nitani, H. Magnetocaloric effect of rare earth mono-nitrides, TbN and HoN. *J. Alloy. Compd.* **376**, 17–22 (2004).
49. Ćwik, J., Koshkid'ko, Y., Nenkov, K., Tereshina, E. A. & Rogacki, K. Structural, magnetic and magnetocaloric properties of $HoNi_2$ and $ErNi_2$ compounds ordered at low temperatures. *J. Alloy. Compd.* **735**, 1088–1095 (2018).
50. Zhang, H. et al. Large reversible magnetocaloric effects in ErFeSi compound under low magnetic field change around liquid hydrogen temperature. *Appl. Phys. Lett.* **102**, 092401 (2013).
51. Xu, Y., Yamazaki, M. & Villars, P. Inorganic materials database for exploring the nature of material. *Jpn. J. Appl. Phys.* **50**, 11RH02 (2011).